ORIGINAL ARTICLE

Intravenous route to choroidal neovascularization by macrophage-disguised nanocarriers for mTOR modulation

Weiyi Xia[a,†], Chao Li[b,†], Qinjun Chen[b], Jiancheng Huang[a], Zhenhao Zhao[b], Peixin Liu[b], Kai Xu[a], Lei Li[a], Fangyuan Hu[a], Shujie Zhang[a], Tao Sun[b], Chen Jiang[b,*], Chen Zhao[a,*]

[a]Department of Ophthalmology and Vision Science, Eye & ENT Hospital, Shanghai Medical School, Fudan University, Shanghai 200031, China
[b]Key Laboratory of Smart Drug Delivery, Ministry of Education, Department of Pharmaceutics, School of Pharmacy, Fudan University, Shanghai 201203, China

Abstract Retinal pigment epithelial (RPE) is primarily impaired in age-related macular degeneration (AMD), leading to progressive loss of photoreceptors and sometimes choroidal neovascularization (CNV). mTOR has been proposed as a promising therapeutic target, while the usage of its specific inhibitor, rapamycin, was greatly limited. To mediate the mTOR pathway in the retina by a noninvasive approach, we developed novel biomimetic nanocomplexes where rapamycin-loaded nanoparticles were coated with cell membrane derived from macrophages (termed as MRaNPs). Taking advantage of the macrophage-inherited property, intravenous injection of MRaNPs exhibited significantly enhanced accumulation in the CNV lesions, thereby increasing the local concentration of rapamycin. Consequently, MRaNPs effectively downregulated the mTOR pathway and attenuate angiogenesis in the eye. Particularly, MRaNPs also efficiently activated autophagy in the RPE, which was acknowledged to rescue RPE in response to deleterious stimuli. Overall, we design and prepare macrophage-disguised rapamycin nanocarriers and demonstrate the therapeutic advantages of employing biomimetic cell membrane materials for treatment of AMD.

*Corresponding authors. Fax: +86 21 64377134 (Chen Zhao), +86 21 51980079 (Chen Jiang).
E-mail addresses: jiangchen@shmu.edu.cn (Chen Jiang), dr_zhaochen@163.com (Chen Zhao).
†These authors made equal contributions to this work.

1. Introduction

Age-related macular degeneration (AMD) is one of the leading causes of irreversible blindness among the elderly population in many countries, dramatically affecting the quality of life of patients[1]. Retinal pigment epithelium (RPE) is a monolayer of polarized cells located between the retinal photoreceptor layer and the choroidal vasculature layer. Primary dysfunction of RPE triggers a serious of detrimental inflammation and initiates the degeneration of photoreceptors, leading to AMD progression[2]. Furthermore, in the late stage, due to excessive pro-angiogenic cytokines secreted by RPE, pathologic choroidal neovascularization (CNV) sprouts from the choroidal vasculature through the Bruch's membrane into the subretinal space (Fig. 1A), leading to serious consequences such as hemorrhage, exudation, retinal edema, RPE detachment and secondary fibrovascular

scarring[3]. Indeed, CNV accounts for the majority of cases of blindness in AMD patients[4].

Among all the ageing hallmarks of AMD, inflammation has long been considered a major pathway that ceaselessly recurs and integrates with other processes in the manifestation of this disorder. Activation of inflammatory response promotes RPE cells to secrete proinflammatory cytokines, such as IL-1β, tumor necrosis factor-α (TNF-α), IL-6 and IL-8[5]. In response to the local high level of cytokines, endothelial cells in the choroid are activated, which is characterized by increased expression of adhesion molecules. By making contact with the adhesion molecules, more inflammatory cells enter the inflamed tissue and subsequently participate in RPE degeneration and CNV expansion. Generally, RPE has been considered at the central site of pathological alterations in AMD, the abnormalities of which activate CNV formation and contribute to inflammatory cell infiltration[6]. The development of CNV, in turn,
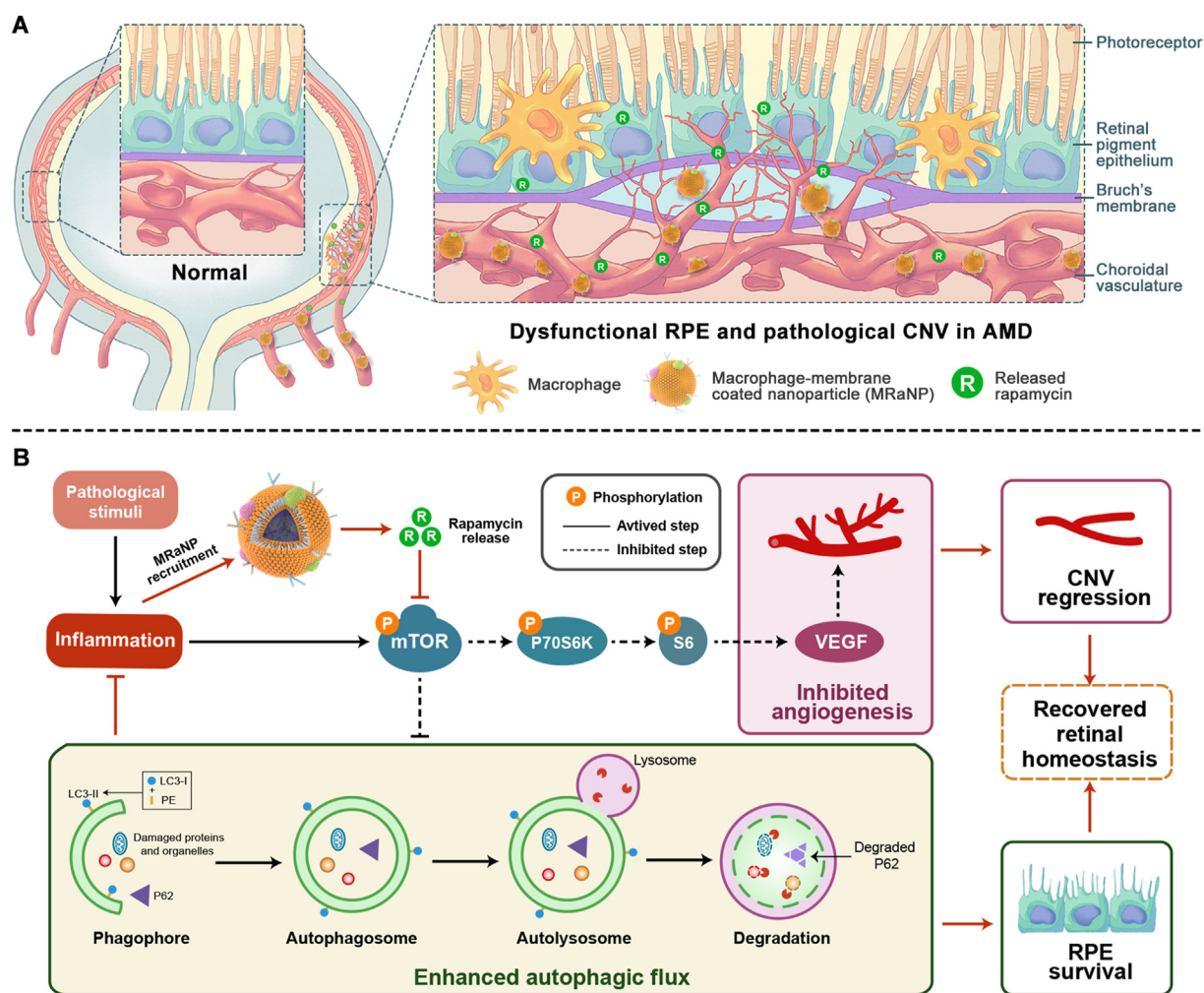

Figure 1 Schematic diagram. (A) Illustration of macrophage-disguised nanoparticles (MRaNPs) targeting choroidal neovascularization *via* the intravenous route. (B) Illustration of retinal homeostasis modulation by MRaNPs *via* the mTOR signaling pathway.

exacerbates RPE deterioration and boosts inflammation, establishing a vicious circle that aggravates the progress of AMD.

The mammalian target of rapamycin (mTOR) is a highly conserved protein kinase that regulates basic cellular functions such as cell growth, proliferation, metabolism and autophagy[7]. Previous studies have revealed the key role of mTOR signaling pathway in AMD pathophysiology. Sustained mTOR activation induces RPE dedifferentiation and secondary photoreceptor loss[8]. Meanwhile, the mTOR signaling pathway acts as a critical upstream stimulator of vascular endothelial growth factor (VEGF), a potent pro-angiogenic factor involved in the pathological process of CNV[9,10]. As expected, mTOR inhibition is advantageous to enhancing autophagy, which is dysregulated in AMD, and to suppressing inflammation[11,12]. Taken together, the regulatory effects of mTOR pathway overlap with multiple pathogenic processes in AMD, promoting it an attractive therapeutic target for the disease. However, current established treatment only targets the downstream VEGF. Despite the great success of anti-VEGF therapy, the frustrating fact is that only 1/3 patients obtain vision improvement, and 1/3 patients respond poorly to this therapy[13,14]. In addition, long-term or even life-long use of anti-VEGF agents has adverse effects such as geographic atrophy and retinal fibrosis[15,16]. This is largely because anti-VEGF is not sufficient to break the vicious circle between RPE degeneration, CNV development and inflammation, not to mention curing AMD.

Intravitreal administration is the most common drug delivery approach to posterior ocular segment, either for pharmacotherapy (e.g., anti-VEGF agents) or for gene therapy[17]. However, these therapeutic strategies usually require repeated intravitreal injections, which involve serious unintended side effects such as ocular hemorrhage, intraocular pressure elevation, endophthalmitis, and ocular inflammation[18]. The situation is similar for the specific mTOR antagonist, rapamycin (Rapa). Rapa has been of great interest to researchers for many years, as extensive research has shown the dramatic efficacy of Rapa in ameliorating CNV and protecting RPE via its versatile pharmacological effects, including anti-inflammation, anti-proliferation, anti-migration, and inducing autophagy[19,20]. Nevertheless, previous clinical trials reported that intravitreal injection of Rapa had its problems. Apart from those intravitreal injection-related as mentioned above, it has adverse effects such as anterior uveitis, sterile endophthalmitis and cataract, which are mainly due to the drug toxicity from burst drug release[21−24]. On the other hand, systemic administration of Rapa is normally difficult to take effect for ocular diseases, because of its poor accumulation in the lesion sites, weak penetration through blood−retinal barrier (BRB) and rapid clearance by reticuloendothelial system (RES) during circulation.

In the inflammatory microenvironment of AMD, numerous peripheral circulation-derived inflammatory cells, the majority of which are macrophages, are recruited to regions of RPE atrophy and CNV[25,26]. The macrophages presented in these regions do not enter into the eye in healthy state, but can infiltrate into the diseased retina with impaired BRB functions[6,27,28]. By following the increasing chemokine gradient, macrophages leave the peripheral circulation, travel towards the damaged tissue and finally reach the site of inflammation[29]. Herein, the innate inflammation-directed chemotactic ability macrophages have specially captured our attention, which has been implicated to be attributed to the proteins on the membrane[30]. We presume that macrophage membrane-coated nanocarriers are hopeful to satisfy the needs of ocular delivery, since the membrane modification could disguise the nanocarriers as macrophages so as to evade the RES, and specifically reach and accumulate in the AMD lesions through the BRB via protein interactions between nanocarriers and CNV (Fig. 1A). As a result, higher local concentration of Rapa can be achieved to modulate the mTOR signaling in retina, thus treating AMD more effectively via an upstream target of VEGF (Fig. 1B).

In this study, as shown in Fig. 2A, we first incorporated Rapa into poly (lactic-co-glycolic) acid (PLGA), a US Food and Drug Administration (FDA)-approved biodegradable and biocompatible material to form Rapa-PLGA cores (RaNPs). Afterwards, we integrated the macrophage membrane-derived vesicles (M-vesicles) onto RaNPs to fabricate the macrophage-membrane-based core−shell structured nanocomplexes (MRaNPs). The biomimetic nanoparticles showed preferential accumulation in the inflamed CNV lesions after tail vein injection in a laser-induced CNV (LCNV) mouse model, and the subsequent released Rapa attenuate the development of angiogenesis. Taking advantage of the proximity of the choroidal vasculature to the RPE, MRaNPs also exerted an anti-inflammation and potential RPE-protective effect in the inflammatory microenvironment by enhancing autophagy.

2. Materials and methods

2.1. Cell culture

RAW 264.7 cells and human umbilical vein endothelial cells (HUVECs) were cultured in Dulbecco's modified Eagle's medium (DMEM, Gibco, Grand Island, NY, USA). APRE-19 cells were cultured in Dulbecco's modified Eagle's medium/nutrient mixture F-12 (DMEM/F-12, Gibco). The medium was supplemented with 10% fetal bovine serum (FBS, Gibco), 1% penicillin−streptomycin (Thermo Fisher Scientific, Waltham, MA, USA). All cells were cultured at 37 °C with 5% CO_2.

2.2. Preparation of RaNPs

RaNPs were prepared according to a previously described method with minor modification[31]. In brief, carboxy-terminated 50:50 PLGA (10 mg, MW = 100,000, Daigang Biology, Jinan, China) polymer and Rapa (MedChemExpress, Princeton, NJ, USA) in 1 mL of dimethyl sulfoxide (DMSO) was added dropwise to 3 mL of deionized water under magnetic stirring. The obtained suspension was subjected to dialysis (3500 MWCO, Thermo Fisher Scientific) against 5 L of deionized water for 24 h to remove the free Rapa and DMSO. The collected RaNP solution was lyophilized and stored at −20 °C for further study. To prepare fluorescently labeled RaNPs, 0.1 wt% 1,1′-dioctadecyl-3,3,3′,3′-tetramethylindocarbocyanine perchlorate (DiI, Meilun Biological Technology, Dalian, China) was loaded into the polymer solution.

2.3. Preparation of M-vesicles and MRaNPs

M-vesicles were derived in accordance with previously described protocols with some modification[32]. RAW 264.7 cells at full confluence were isolated from the culture dish and washed with PBS three times. Next, the cells were resuspended in ice-cold 0.1 × TM buffer (Sangon Biotech, Shanghai, China) containing protease and phosphatase inhibitor cocktail (Thermo Fisher Scientific). The cell suspended solution was repeatedly grinded by a Dounce homogenizer for 20 passes to disrupt the cells, followed by centrifugation at 3200×g for 5 min (ST 16, Thermo Fisher
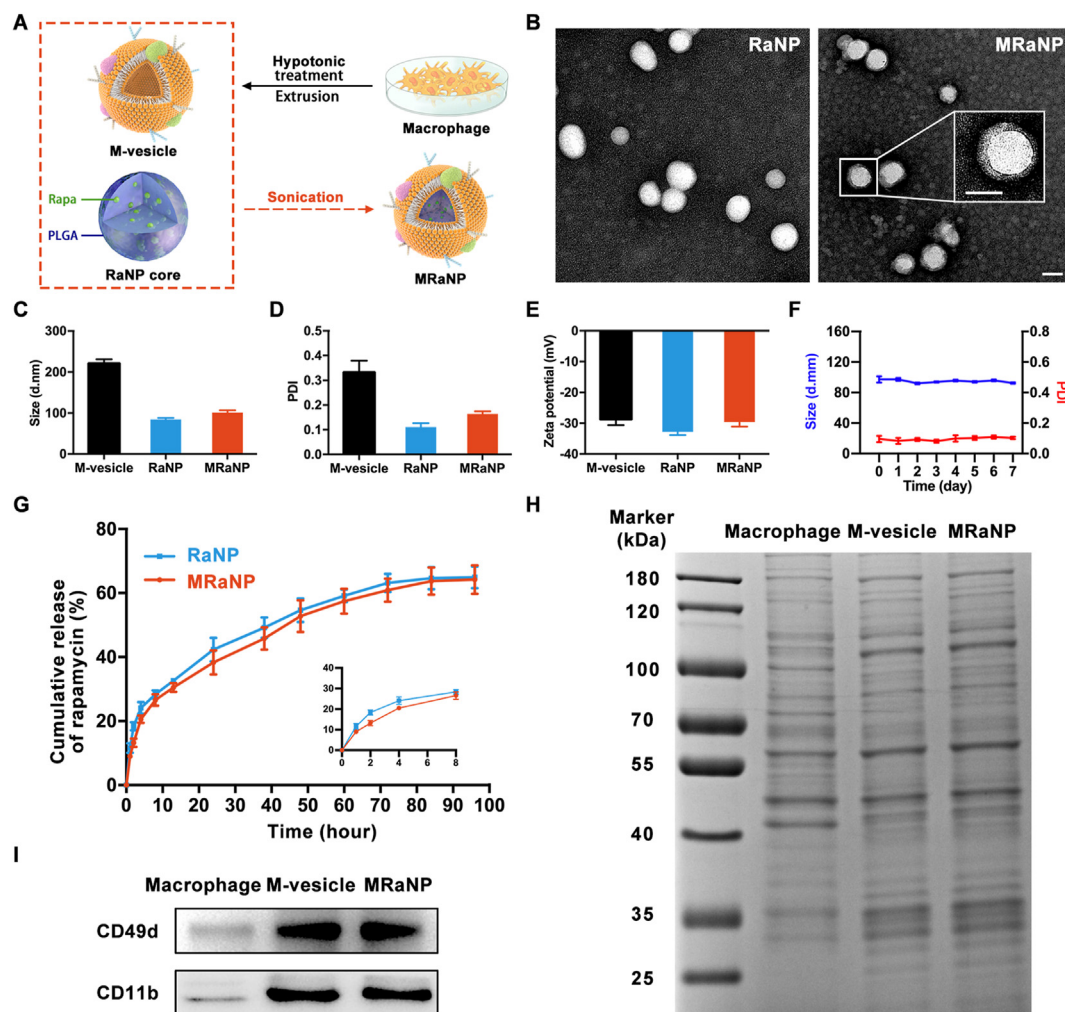
Figure 2 Characterization of MRaNPs. (A) Scheme of preparation process of MRaNP. (B) TEM images of RaNPs (left) and MRaNPs (Right). Insert: a zoomed-in view of a single MRaNP. Scale bar = 100 nm. (C to E) Hydrodynamic size, PDI and Zeta potential of M-vesicles, RaNPs and MRaNPs ($n = 3$). (F) Measurements of size and PDI of MRaNPs over 7 d ($n = 3$). (G) Drug release from RaNPs and MRaNPs in PBS at 37 °C over the course of 96 h ($n = 3$). (H) SDS-PAGE protein analysis of macrophage cell lysate, M-vesicles and MRaNPs. (I) WB analysis for CD49d and CD11b in macrophage cell lysate, M-vesicles and MRaNPs.

Scientific). The pellet was removed and the supernatant was centrifuged at 20,000×g for 25 min (Thermo Fisher Scientific). The upper supernatant was collected again and centrifuged at 100,000×g for 60 min (CP100NX, Hitachi, Tokyo, Japan). The eventual pellet was collected, dispersed in water and extruded through 400 and 200 nm polycarbonate porous membranes by an Avanti mini extruder (LF-1, Avestin, Ottawa, Canada) to generate M-vesicles. M-vesicle material was stored at −80 °C for future study. To prepare MRaNPs, the M-vesicles were mixed with the as-prepared RaNPs at a membrane protein-to-PLGA weight ratio of 1:1. The mixture was sonicated for 3 min using a bath sonicator. The obtained MRaNPs were stored at 4 °C until use.

2.4. Characterization of nanoparticles

The morphology of RaNP and MRaNP was visualized using transmission electron microscopy (TEM Talos L120C G2, Thermo Fisher Scientific). The size, polydispersity index (PDI) and Zeta potential of M-vesicles, RaNPs and MRaNPs were determined by dynamic light scattering (DLS, ZEN 3600 Zetasizer, Malvern

Instruments, Malvern, UK). The stability of MRaNPs in PBS was tested by mixing 1 mg/mL of MRaNPs in water with 2 × PBS (pH = 7.4) at a volume ratio of 1:1. Protein profile of macrophages, M-vesicles and MRaNPs were analyzed by sodium dodecyl sulfate-polyacrylamide gel electrophoresis (SDS-PAGE). Briefly, all samples were normalized to equal protein concentrations by a BCA assay (Beyotime, Shanghai, China). Afterwards, 20 μg of each sample was loaded onto a 10% SDS-PAGE gel (Beyotime). Finally, the SDS-PAGE gel was stained with Coomassie blue for visualization. To further detect the expression of CD49d and CD11b on macrophages, M-vesicles and MRaNPs, Western blotting (WB) analysis was performed as described below except that the primary antibodies used were CD49d (1:1000, Abcam, Cambridge, UK) and CD11b (1:1000, Abcam).

2.5. Drug loading and in vitro drug release study

To determine the loading efficiency (LE) and drug encapsulation efficiency (EE) of RaNP, the RaNP lyophilized powder was weighed and then dissolved in acetonitrile to collapse the

nanoparticles. Next, the concentration of the encapsulated Rapa was quantified by a high performance liquid chromatography (HPLC) method[33]. The LE and EE were calculated using the following Eqs. (1) and (2):

$$LE(\%) = \frac{\text{Weight of Rapa encapsulated in RaNP}}{\text{Weight of RaNP}} \times 100 \quad (1)$$

$$EE(\%) = \frac{\text{Weight of Rapa encapsulated in RaNP}}{\text{Weight of total Rapa}} \times 100 \quad (2)$$

The *in vitro* release profile of Rapa from RaNPs and MRaNPs was plotted over 96 h. Briefly, 1 mL of RaNP and MRaNP solutions were added to disposable polypropylene cups (3500 MWCO, Thermo Fisher Scientific) suspended in a 15-mL centrifuge tube containing release buffer while shaken at 50 rpm in 37 °C bath. To meet the sink condition, the release buffer used was PBS (pH = 7.4) supplemented with 0.1% tween 80. At predetermined time intervals, an aliquot of solution (100 μL) was collected from the external centrifuge tube and an equivalent amount of fresh release buffer was added. The concentration of released Rapa was measured by HPLC[33].

2.6. Cellular uptake by HUVECs

HUVECs were seeded in 12-well plates. When reaching a confluence of 80%−90%, DiI-labeled RaNP or MRaNP were added with a concentration of 20 ng of DiI in 500 μL of PBS per well (pH = 7.4). After incubation for 0.5, 1, 2 or 4 h, the cells were washed three times with PBS, and fixed with 4% paraformaldehyde (PFA). Then the cells were imaged using a fluorescence microscope (CKX53, Olympus, Osaka, Japan). In addition, the cells from parallel samples were detached from the plate with 0.25% trypsin−EDTA, suspended in PBS, and then analyzed by a flow cytometer (cytoFLEX, Beckman Coulter, Indianapolis, IN, USA). To further explore the cellular uptake under inflammatory conditions, HUVECs were treated with TNF-α (50 ng/mL, ProteinTech, Chicago, IL, USA) for 12 h, followed by incubation with different nanoparticles for another 4 h. The results were analyzed by a flow cytometer.

2.7. Cellular uptake mechanism exploration

HUVECs were seeded in 14 mm glass-bottom dishes (NEST Biotechnology, Wuxi, China). When achieving an 80%−90% cell density, the cells were treated with TNF-α (50 ng/mL) for 12 h. DiI-labeled RaNPs, MRaNPs or red blood cell membrane-coated RaNPs (RRaNPs) were then added and incubated for 4 h. Here, the RRaNPs were prepared in accordance with the method as previously described[31]. After the incubation, the cells were washed with PBS, fixed with 4% PFA for 15 min and blocked with 5% Bovine serum albumin (BSA, Sigma−Aldrich, St. Louis, MO, USA) for 30 min. Then, primary antibody against intercellular adhesion molecule 1 (ICAM-1, 1:100, Abcam) or vascular cell adhesion molecular 1 (VCAM-1, 1:100, Abcam) was added and incubated at 4 °C overnight, followed by Fluorescein Isothiocyanate (FITC)-labeled secondary antibody (1:1000, Abcam) and 4′,6-diamidino-2-phenylindole (DAPI) staining. Cells were visualized by confocal laser scanning microscopy (CLSM, LSM710, Zeiss, Oberkochen, Germany).

2.8. Cell proliferation detection by Ki67 staining

HUVECs were seeded in 24-well plates, cultured to a 70%−80% confluence and exposed to VEGF (10 ng/mL, R&D Systems, Minneapolis, MN, USA) for 12 h, followed by the treatment with free Rapa, RaNPs or MRaNPs (Rapa was normalized to 0.1 μmol/L) for 48 h. The cells treated with PBS were served as a control. After treatment, the cells were fixed with 4% PFA, permeabilized with PBS containing 0.15% Triton X-100 and blocked with 5% BSA in turn. Subsequently, the cells were incubated with primary antibody against Ki67 (1:200; Abcam) at 4 °C overnight, followed by incubation with AlexaFluor-488-conjugated secondary antibody and DAPI staining sequentially. The cells were photographed using a fluorescence microscope (Olympus).

2.9. Scratch wound migration assay

HUVECs were seeded in 24-well plates and allowed to reach a 70%−80% confluence. A pipette tip was employed to mark out a scratch on the adhering cells, and the cells were washed with PBS to remove the debris. After exposure to free Rapa, RaNPs or MRaNPs (Rapa was normalized to 0.1 μmol/L) or to PBS as control for 24 h, the cell migration was recorded by a bright-field microscope (Olympus). Finally, the scratch areas were calculated by the ImageJ software.

2.10. Tube formation assay

Each well of the pre-chilled 96-well plate was coated with 50 μL growth factor-reduced matrigel (BD Biosciences, San Jose, CA, USA), followed by incubation for 30 min at 37 °C for gelation. HUVECs in 100 μL of required medium were then seeded onto the matrigel at a density of 20,000 cells per well. After 4 h of incubation, the capillary-like network structure was viewed under a bright-field microscope (Olympus). The capillary tube length was quantified by measuring the total branching length using ImageJ.

2.11. Intracellular drug release behavior

ARPE-19 cells were seeded in 14-mm glass-bottom dishes. Upon reaching an 80%−90% cell confluence, the media were replaced with fresh media containing DiI-labeled MRaNPs (10 ng/mL), and the cells were cultured for additional 0−2 h, respectively. Next, the cells were washed with PBS, fixed with 4% PFA, permeabilized with 0.15% Triton X-100 and blocked with 5% BSA, followed by counter-staining with LAMP1 (1:20, Abcam) at 4 °C overnight, the corresponding FITC-conjugated secondary antibody and DAPI in sequence. The cells were observed with CLSM (Zeiss) through a 63 × oil immersion lens.

2.12. Cytotoxicity detection by CCK-8 assay

ARPE-19 cells were seeded in a 96-well plate with a density of 5000 cells per well and maintained in the culture medium for 12 h. The cells were washed with PBS and fresh cell culture mediums containing PBS as control or different concentrations of free Rapa, RaNPs or MRaNPs (0.1, 0.5, or 2 0 μmol/L, the equivalent concentration of Rapa) were added to the cell culture plate (100 μL per well), followed by incubation for another 24 h. The cells were

washed, and 100 μL CCK-8 solution (10%, Beyotime) was added. The cells were incubated for another 2 h at 37 °C, and the 450 nm absorbance of each well was measured using a microplate reader for calculating the cell viability in each well.

2.13. Measurement of cytokines

ARPE-19 cells were seeded in 6-well plates and cultured to an 80%−90% confluence. The harvested cells were treated with lipopolysaccharide (LPS, 10 μg/mL, ProteinTech) for 12 h, and incubated with PBS, free Rapa (0.1 μmol/L), or MRaNPs (0.1 μmol/L of Rapa) along or in combination with Bafilomycin A1 (Baf, 0.1 μmol/L, MedChemExpress) for another 12 h. The culture supernatant from each sample was then collected. The concentrations of IL-6 and IL-8 were valued by enzyme-linked immunosorbent assays (ELISA) kits (Abcam) according to the manufacturer's instructions.

2.14. Investigation of cell autophagy by immunofluorescence staining

ARPE-19 cells were seeded in glass-bottom dishes and incubated until an 80%−90% confluence. Cells were exposed to LPS (10 μg/mL) for 12 h, followed by PBS, free Rapa (0.1 μmol/L) or MRaNP (0.1 μmol/L) treatment for 12 h. After that, the cells were washed and incubated with 10 μmol/L Acridine Orange (AO, Sigma−Aldrich) for 30 min before the observation with CLSM (Zeiss). To investigate the autophagic flux, the cells from parallel samples were fixed, blocked and incubated with primary antibody against LAMP1 (1:20) and LC3 (1:800, Abcam) at 4 °C overnight, followed by AlexaFluor-488-conjugated secondary antibody and AlexaFluor-594-conjugated secondary antibody, respectively. After DAPI staining, the cells were photographed with CLSM (Zeiss).

2.15. Animals and establishment of the LCNV mouse model

Animal experiments were carried out in accordance with the guidelines approved by Institutional Animal Care and Use Committee (IACUC) of Eye & ENT Hospital of Fudan University. All mice used in this study were male eight-week-old C57/BL6 mice weighing 22−24 g from Shanghai Slac Laboratory Animal Co., Ltd. (Shanghai, China). The mice were carefully maintained under specific-pathogen-free laboratory conditions under a 12 h−12 h light−dark cycle. The establishment of LCNV mouse model was performed according to a previously established protocol[34]. Mice were anesthetized and their pupils were then dilated. To induce CNV, four laser spots surrounding the optic disc were generated with an Argon laser pulse (Micron IV, Phoenix Research Laboratories, Pleasanton, CA, USA). Both eyes of the mice received laser treatment. The formation of a white bubble confirmed the disruption of Bruch's membrane, as well as a successful laser impact. Laser parameters applied in this work were set with an 100 ms of duration, 110 mW of power and 100 μm of spot size.

2.16. Animal experimental design

To test the CNV-targeting ability of MRaNPs in LCNV mice, on Day 5 after the laser treatment, DiI-labeled RaNPs or MRaNPs (DiI was normalized to 1 μg) was injected into the tail vein of mice. 4 H later, the mice were sacrificed. The RPE-choroid

complex layers were separated from the enucleated mouse eyes for the IB4 staining. To study the natural time-course of CNV formation and macrophage infiltration in LCNV mice, mice were sacrificed on Days 1, 3, 5, 7, and 14 after the laser treatment. The RPE-choroid complex (RCC) layers were collected for IB4 and F4/80 staining. To evaluate the therapeutic effect, the mice were randomized into four groups after the laser treatment. The mice in the saline group served as the control group, while the other three groups were daily treated with free Rapa, RaNPs or MRaNPs (Rapa was normalized to 1 mg/kg) *via* tail vein injection from Day 2 to Day 7. On Day 8, the mice were sacrificed for further investigation. The separated RCC layers were used for either immunofluorescence staining or WB analysis. For the biosafety evaluation, the blood serum was collected for blood chemistry analysis. The retina tissues and the major organs (heart, liver, spleen, lung and kidney) were processed for histological hematoxylin and eosin (H&E) staining.

2.17. Immunofluorescence of flat-mounted RCC

After the mice were euthanized, their eyes were enucleated and then fixed with 4% PFA for 1 h at room temperature. The cornea and lens were discarded, and the neuroretina was carefully separated from the RCC *via* blunt dissection. The RCC was then permeabilized with 0.15% Triton X-100 in PBS for 20 min and blocked with 5% BSA in PBS for 1 h at room temperature. To label the CNV lesions, the RCC was incubated with FITC-conjugated isolectin-B4 (IB4, 10 μg/mL, Sigma−Aldrich) at 4 °C overnight. After washing with PBS, the whole RCC was flat-mounted with antifade mounting medium (Thermo Fisher Scientific). CNV lesions were photographed under a fluorescence microscope (Olympus) and the areas (μm^2) of lesions were quantified using the ImageJ software in masked fashion. Lesions with obvious failure or hemorrhage were excluded for analysis[35]. Immunofluorescence staining of F4/80 (1:100, Abcam) or p-mTOR (1:100, Abcam) was performed as that of IB4 except that fluorescent-labeled secondary antibodies were added.

2.18. WB analysis

RCC tissues or cells were lysed in RIPA buffer (Beyotime) containing protease and phosphatase inhibitor cocktail. The lysate solution was centrifuged at $13,000 \times g$ for 10 min at 4 °C (Thermo Fisher Scientific) and the supernatant was collected to obtain the protein. The protein concentrations were quantitated by the BCA assay. Then, 20 μg of each protein sample was separated on an SDS-PAGE gel and transferred onto the PVDF membranes (Millipore, St. Louis, MO, USA). After being blocked with 5% skimmed milk in tris-buffered saline with 0.1% Tween-20 (TBST), the membranes were probed with primary antibodies at 4 °C overnight. Subsequently, horseradish peroxidase (HRP)-conjugated secondary antibodies (Beyotime) were incubated for 2 h. Specific bands were finally visualized using Immobilon Western Chemiluminescent HRP Substrate (Millipore). The primary antibodies used were as followed: VEGFA (1:1000), ICAM-1 (1:2000) and VCAM-1 (1:2000) from Abcam, and mTOR (1:1000), p-mTOR (Ser2448, 1:1000), P70S6K (1:1000), p-P70S6K (Thr389, 1:1000), S6 (1:1000), p-S6 (Ser240/244, 1:1000), P62 (1:1000), Beclin-1 (1:1000), LC3 (1:1000), GAPDH (1:1000) and β-Actin (1:1000) from Cell Signaling Technology (Danvers, MA, USA).

2.19. Statistical analysis

All data were analyzed by GraphPad Prism Version 7.0 (GraphPad Software, San Diego, CA, USA) or ImageJ software, and presented as means $\pm$ standard deviation (SD). The statistical significance was evaluated by one-way analysis of variance (ANOVA) or Student's t-test. The significance level was defined as $^*P < 0.05$, $^{**}P < 0.01$, $^{***}P < 0.001$ and $^{****}P < 0.0001$.

3. Results

3.1. Preparation and characterization of MRaNPs

Considering the poor solubility of Rapa in water, the polymer cores were prepared using PLGA as a hydrophobic drug carrier to encapsulate Rapa. The optimization of the weight ratio of PLGA and Rapa was implemented by incorporating Rapa with PLGA at different weight ratios (5%, 10% and 15%). The maximum Rapa incorporation ratio was 10%, with an average LE and EE of 6.9% and 73.9%, respectively. When more Rapa was incorporated, the aggregation of RaNPs was observed (Supporting Information Fig. S1).

Macrophages were disrupted by hypotonic treatment, then centrifuged to isolate and purify the macrophage membrane. The purified macrophage membrane was extruded through polycarbonate porous membranes to obtain M-vesicles. Next, RaNPs were wrapped in the extracted M-vesicles using a sonication method (Fig. 2A). The successful cloaking of RaNP with M-vesicle was verified using TEM. As displayed in Fig. 2B, MRaNP presented a clear core–shell structure, in which the RaNP core was wrapped with an approximately 8 nm-thickness shell. Correspondingly, DLS measurements revealed that the diameter of RaNPs increased from 84.3 ± 3.5 nm to 101.3 ± 5.1 nm after membrane coating. Such a diameter increase of about 17 nm was consistent with the addition of a bilayer cell membrane onto the surface of the RaNP core (Fig. 2C)[32]. The PDI increased slightly from 0.111 ± 0.016 to 0.164 ± 0.011 (Fig. 2D). The surface Zeta potential changed from -32.8 ± 1.1 to -29.6 ± 1.5 mV, similar to that of the natural M-vesicles of -28.7 ± 1.9 mV (Fig. 2E). Notably, nanoparticles with negative surface charge were documented to be more favorable than cationic nanoparticles during penetration through the choroid and retina[17]. The particle size and PDI of MRaNPs were monitored by DLS for one week in PBS at pH 7.4, and turned out to be unchanged, indicating the favorable stability of MRaNPs over time (Fig. 2F). Both RaNPs and MRaNPs exhibited a sustained release of encapsulated Rapa in PBS (pH 7.4) at 37 °C, which could guarantee minimal leakage of the drug when traveling along circulation (Fig. 2G). Besides, the drug release profile of MRaNPs was slightly slower than that of RaNPs, which might be ascribed to the wrapping of the membrane served as a diffusion barrier.

Since the retention of M-vesicle proteins on MRaNPs was indispensable for its biofunctionalization, the protein profile of Macrophages, M-vesicles and MRaNPs was typically determined by SDS-PAGE and visualized by Coomassie blue. As shown in Fig. 2H, the protein composition of MRaNPs was modulated when compared to macrophages (including intracellular proteins), but was highly consistent with that of M-vesicles, thus confirming the preservation of macrophage membrane proteins on RaNPs throughout the fabrication process.

In the choroid and aqueous humor of AMD patients, there is an overexpression of ICAM-1 and VCAM-1[36−38]. Besides, the evidence in the literature suggested that macrophages could actively adhere to the endothelial cells *via* the interactions between adhesion molecules, such as CD11b-ICAM-1 and CD49d-VCAM-1[39−42]. To further identify these two potential functional proteins on MRaNPs, the expression of CD11b and CD49d on macrophages, M-vesicles and MRaNPs were determined by WB analysis. As presented in Fig. 2I and Supporting Information Fig. S2, there was a remarkable enrichment of CD11b and CD49d in M-vesicles and MRaNPs, which also substantiated the translocation of macrophage membrane proteins onto MRaNPs.

3.2. In vitro cellular uptake by endothelial cells and the potential mechanism

It is acknowledged that endothelial cells are major players contributing to ocular neovascular disorders[43]. To determine whether membrane coating altered the uptake of nanoparticles by endothelial cells, we incubated DiI-labeled RaNPs or MRaNPs with HUVECs and performed time–lapse studies utilizing flow cytometer and fluorescence microscope. In the resting state (without pathogen stimulation), both RaNPs and MRaNPs were internalized by HUVECs in a time-dependent manner. Furthermore, the cellular uptake of MRaNPs by HUVECs was significantly higher than that of RaNPs (Fig. 3A and Supporting Information Fig. S3), which was probably attributed to the modification of adhesion molecules on the exterior of MRaNPs and the resultant active molecular interactions between MRaNPs and HUVECs.

At the beginning of inflammation, TNF-α plays an important role in activation of endothelial cells[44]. To further determine the binding ability of MRaNPs to inflamed vessel and investigate the potential mechanism, the HUVECs were treated with the pro-inflammatory cytokine TNF-α so as to establish a model of inflamed vessel, while the untreated HUVECs were applied as control. Afterwards, HUVECs were incubated with DiI-labeled RaNPs, DiI-labeled MRaNPs, or DiI-labeled RRaNPs for 4 h. As shown in Supporting Information Fig. S4, the expression of ICAM-1 and VCAM-1, the counter-ligand for CD11b and CD49d, respectively, was significantly increased in response to TNF-α stimulus. Similar results were also revealed in the immunocytochemistry study (Fig. 3B and C, green). Furthermore, the cellular uptake of MRaNPs by HUVECs (red) and colocalization of MRaNPs with ICAM-1/VCAM-1 (yellow, also denoted by white arrowheads) were both much apparently stronger than those of RaNPs or RRaNPs, which exhibited the specific binding capacity of MRaNPs to HUVECs (Fig. 3B and C). Consistently, quantitative study by flow cytometry substantiated that both macrophage membrane modification and inflammatory stimuli significantly accelerated MRaNP uptake by HUVECs (Supporting Information Fig. S5). Because there was a lack of protein expression of CD11b and CD49d on the membrane of RBCs, these results suggested that the enhanced binding capacity of MRaNPs to HUVECs was due to the specific adhesion molecules, and the interactions between CD11b-ICAM-1 and CD49d-VCAM-1 might be the two functional pathways. Collectively, macrophage membrane coating enhanced the cellular uptake of MRaNPs in activated endothelial cells, indicating a feasible strategy for CNV-targeting drug delivery in AMD.
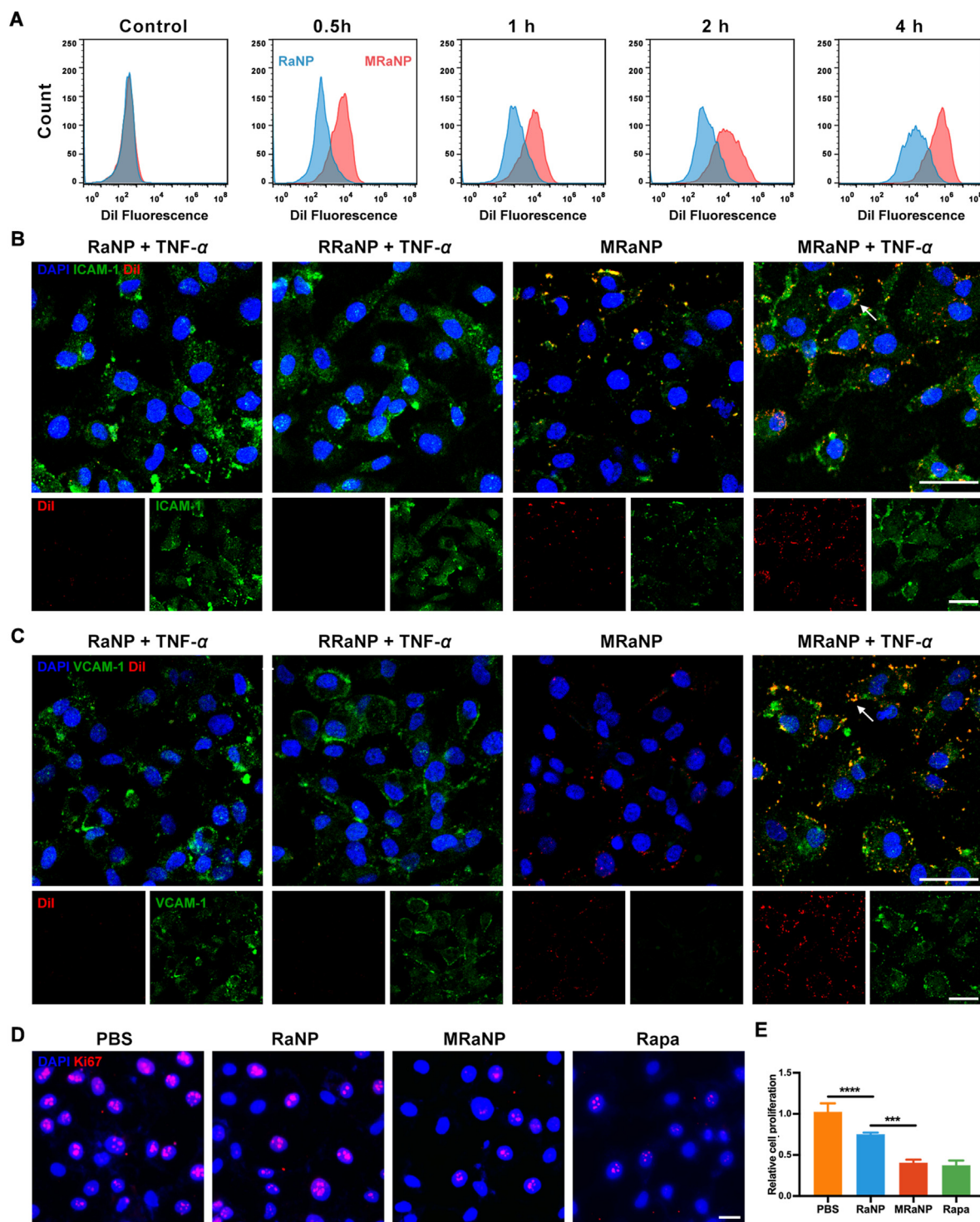
Figure 3 *In vitro* binding and anti-angiogenic effect of MRaNPs. (A) Cellular uptake of DiI-labeled RaNPs and MRaNPs in HUVECs analyzed by flow cytometry at different time points. (B to C) Representative CLSM images of different DiI-labeled nanoparticles (red), HUVECs (blue), and ICAM-1/VCAM-1 (green) with or without TNF-α treatment. Scale bar = 50 μm. (D) Cell proliferation detected by Ki67 immunofluorescence staining. Scale bar = 20 μm. (E) Quantitation analysis of cell proliferation ($n = 3$, ***$P < 0.001$ and ****$P < 0.0001$).

3.3. *In vitro biological effects on endothelial cell function*

Since more nanoparticles, as well as the encapsulated Rapa, were internalized by HUVECs after membrane coating, the biological effects of MRaNPs on endothelial cell function were then evaluated in terms of proliferation, migration and tube formation. After being incubated with PBS, RaNPs, MRaNPs or free Rapa for 48 h following VEGF exposure, the cell proliferation of HUVECs was detected by Ki67 staining. It showed that the efficiency in inhibiting HUVEC proliferation of MRaNPs was

significantly greater than that of RaNPs, but was comparable to that of free Rapa (Fig. 3D and E). In the scratch migration wound assay, MRaNPs exhibited consistent efficiency in reducing the migration ability of HUVECs to free Rapa, but was superior to RaNPs (Supporting Information Fig. S6). Similarly, the tube formation assay showed that MRaNPs were more effective than RaNPs in inhibiting tube formation of HUVECs (Supporting Information Fig. S7). The above results revealed the favorable anti-angiogenic effects of MRaNPs. Furthermore, the bioactivity of Rapa was indicated to be well kept after being escorted into the modified nanoparticles. Accordingly, the long-acting anti-angiogenic effects of MRaNPs on HUVECs might be owing to its sustained release property and the increased cellular uptake by endothelial cells after membrane coating.

3.4. In vitro cellular uptake by RPE cells and cytotoxicity evaluation

Given the major role of RPE in AMD initiation and progression, the biological effects of MRaNPs on RPE cells were next studied[45]. The intracellular behavior of DiI-labeled MRaNPs in ARPE-19, a human RPE cell line, was first observed by CLSM. As shown in Fig. 4A, MRaNPs (red) and LAMP1 (green, a lysosome marker) displayed strong colocalization (yellow) in the first 0.5 h, whereas after 2 h, the release of MRaNPs from lysosomes to the cytoplasm were observed, indicating the internalization of MRaNPs in ARPE-19 cells via a lysosome-dependent way.

Having confirmed the internalization of MRaNP in ARPE-19, its cytotoxicity was evaluated by the CCK-8 assay. As shown in Supporting Information Fig. S8, free Rapa, MRaNPs or RaNPs at Rapa dose from 0.1 to 0.5 μmol/L hardly affected the viability of ARPE-19 after 24 h incubation, which suggested the nontoxicity and biocompatibility of PLGA and macrophage membrane. Interestingly, although evident cytotoxicity was detected at Rapa dose of 2 μmol/L, it was significantly lower in MRaNP and RaNP group than that in free Rapa group. This was probably ascribed to the sustained drug release property of MRaNPs and RaNPs, which minimized the burst effect and reduced the toxicity of Rapa at high concentrations.

3.5. In vitro anti-angiogenesis and anti-inflammation effect via the mTOR signaling pathway

In AMD pathogenesis, VEGFA was a dominant pro-angiogenic factor primarily derived from RPE cells with the presence of inflammation, triggering and sharpening CNV development. To improve our understanding of ocular inflammation, LPS is widely employed to induce a signaling cascade evoking the production of proinflammatory cytokines in RPE cells[46]. As shown in Fig. 4B and Supporting Information Fig. S9, LPS led to overexpression of VEGFA by ARPE-19 cells, which was significantly alleviated when LPS was co-administered with free Rapa or MRaNPs. As mTOR integrated signals regulating cellular energy and metabolism, and accumulating evidence suggested that the synthesis and secretion of VEGFA was regulated by the mTOR signal pathway, there was a close relationship between mTOR and angiogenesis[47,48]. Therefore, the activation of mTOR pathway was assessed by phosphorylation level of mTOR, and the 70 kDa ribosomal protein S6 kinase (P70S6K) and the S6 ribosomal protein (S6), two most widely used downstream indicators of mTOR pathway activity. As illustrated in Fig. 4B and Fig. S9, the

phosphorylation level of m-TOR (Ser2448), P70S6K (Thr389) and S6 (Ser240/244) was elevated in response to LPS stimulation, and was downregulated by addition of Rapa or MRaNPs. The results revealed the mTOR inhibition effect by MRaNPs. Using the mTOR activator MHY1485, it was further confirmed that the decreased VEGFA expression was due to the inhibition of mTOR pathway by MRaNPs. Collectively, MRaNPs could mediate the LPS-induced mTOR pathway activation and the subsequent overexpression of pro-angiogenic VEGFA in ARPE-19 cells, indicating it to be a hopeful therapeutic intervention to suppress neovascularization.

Autophagy is a major cellular repair process for the removal of damaged organelles and protein aggregates. Abundant researches have revealed that dysfunctional RPE autophagy is associated with the pathophysiology of AMD, and Rapa is a potent autophagy inducer[49]. To investigate the completeness of autophagic flux, ARPE-19 cells were treated with LPS, alone or in combination with MRaNPs. We first detected the formation of autolysosomes, an autophagy marker, by acridine orange (AO) staining[50]. As shown in Fig. 4C, the autophagy activity (red) was not altered in LPS-induced inflammatory condition, but was remarkably upregulated by either Rapa or MRaNP treatment. Since the regulated fusion of autophagosomes and lysosomes was required for eliminating inflammation and could be blocked by LPS due to lysosome dysfunction (Fig. 1B)[51], the enhanced colocalization (yellow, also denoted by white arrowheads) of LAMP1 (green) and autophagosome marker microtubule-associated protein light chain 3 (LC3, red) revealed the restoration of autophagic flux with the presence of Rapa or MRaNPs (Fig. 4D). The results demonstrated that MRaNPs contributed to enhanced autophagy in ARPE-19 cells under inflammatory condition, suggesting its potential role in regulation of inflammation. To confirm this, the in vitro anti-inflammation effect of MRaNPs on ARPE-19 cells was then evaluated by ELISA assays. Consistent with previous studies, stimulation by LPS significantly increased the secretion of IL-6 and IL-8, two pro-inflammatory cytokines playing pivotal roles in AMD pathogenesis[46,52]. The LPS-induced inflammation was alleviated by free Rapa or MRaNPs, which could be reversed by Baf A1, a classic inhibitor for autophagosome-lysosome fusion (Fig. 4E and F). Since the activation of autophagy was reported to prevent cells against deleterious stimuli, such as excessive inflammation, oxidative stress and senescence, we further investigated whether the reduced inflammation was due to the enhanced autophagy by MRaNPs[53–55]. Compared with PBS treatment, WB analysis revealed that LPS led to apparent accumulation of undegraded P62, an autophagy substrate, suggesting the complete autophagic flux was impaired (Fig. 4G and Supporting Information Fig. S10). The addition of free Rapa or MRaNPs significantly enhanced the degradation of P62, indicating the recovery of the complete autophagic flux. To confirm that the improved p62 degradation was truly induced by the recovery of autophagic flux instead of lysosomal disruption, Baf A1 was added along with MRaNPs to block the fusion between autophagosomes and lysosomes. As a result, the presence of Baf A1 reversed the effect of P62 degradation induced by MRaNPs. The conversion of LC3-II from LC3-I was regarded as a critical indicator of autophagic activation. Similar results were observed that MRaNPs increased the ratio of LC3-II to LC3-I, even when the autophagosome-lysosome fusion was blocked by Baf A1, substantiating that the LC3-II accumulation was not resulted from impaired lysosomal degradation (Fig. 4G and Fig. S10). Taken together, the disrupted autophagy was involved in the aggravation
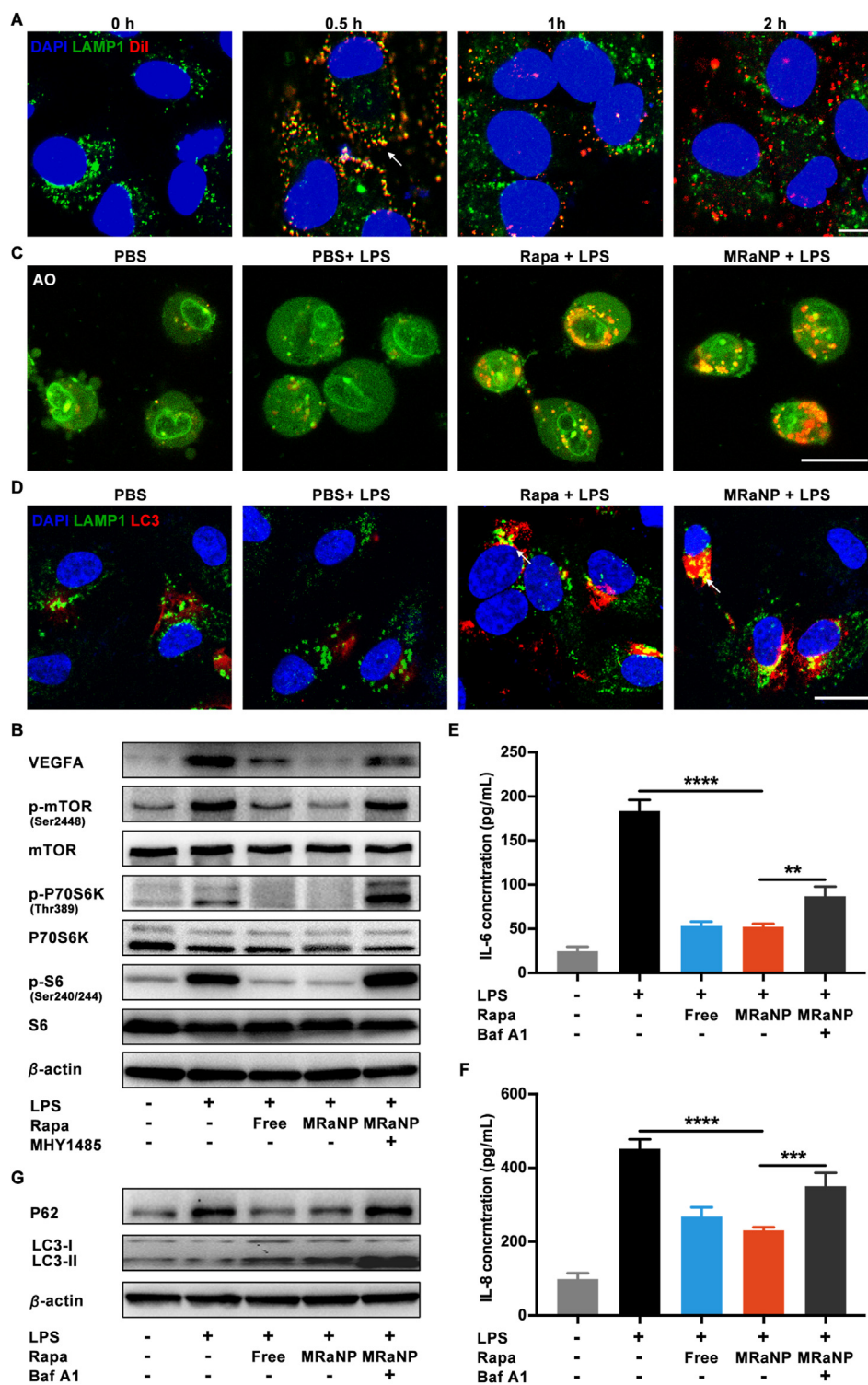
Figure 4 Intracellular behavior and biological effects of anti-angiogenesis and anti-inflammation of MRaNPs in ARPE-19 cells. (A) CLSM images of the intracellular behavior of MRaNPs (blue: DAPI for nucleus; green: LAMP1 for lysosome; red: DiI-labeled MRaNP). Scale bar = 10 μm. (B) WB analysis for VEGFA and the mTOR signaling pathway. (C) CLSM images of autophagy induction stained with AO (green: nucleus; red: autolysosome). Scale bar = 20 μm. (D) CLSM images of autophagic flux (blue: DAPI for nucleus; green: LAMP1 for lysosome; red: LC3 for autophagosome). Scale bar = 20 μm. (E to F) Expression of cytokine IL-6 and IL-8 measured by enzyme-linked immunosorbent assay ($n = 3$, $**P < 0.01$, $***P < 0.001$ and $****P < 0.0001$). (G) WB analysis for autophagy-associated proteins.

of inflammation in ARPE-19 cells, and was rescued by MRaNPs. Since mTOR exerted a negative modulation on autophagy and the blockage of mTOR by MRaNPs had been confirmed[49], it was suggested that MRaNPs could prevent ARPE-19 cells from the LPS-induced inflammation by inducing autophagy *via* inhibiting mTOR, further indicating its RPE-protection effect.

3.6. In vivo CNV-targeting ability

The LCNV mouse model is the most widely used experimental model to study the underlying mechanisms of CNV development and exploit novel pharmacotherapy[34]. Four laser burns can be observed in the successful LCNV models (Supporting Information Fig. S11). Consistent with the results from *in vitro* studies, over-expression of adhesion molecules was observed from the RCC tissues in this inflammation-relied model (Supporting Information Fig. S12). To assess the *in vivo* CNV-targeting ability, MRaNP, DiI-labeled MRaNPs or RaNPs were systemically injected into the LCNV mice *via* the tail vein. Afterwards, the CNV lesions in the flat-mounted RCC tissues were stained with IB4 (green) and the Dil fluorescent signal (red) in CNV lesions was detected by a fluorescence microscope. As presented in Fig. 5A, MRaNPs showed abundant accumulation in the CNV lesions while the accumulation of RaNPs was negligible. A 5.6-fold fluorescent intensity enhancement was observed in the MRaNP group compared to the RaNP group (Supporting Information Fig. S13), confirming that the macrophage membrane modification evaded the phagocytosis of RES and enhanced CNV-targeting ability *in vivo*. Immunostaining of the posterior eye transverse sections (Supporting Information Fig. S14) also demonstrated that MRaNPs (red) were mostly accumulated in the CNV areas (green). As the *in vitro* results demonstrated that MRaNPs exhibited specific binding capacity to endothelial cells with enhanced expression of adhesion molecules, it is reasonable to speculate that vessel endothelial cells in CNV lesions were the special target sites of MRaNPs in this model. If this is the case, once MRaNPs had accumulated in the CNV lesions, Rapa was sustainedly released from MRaNPs, thus achieving an increased local drug concentration to suppress the proliferation and migration of endothelial cells, to reduce inflammatory responses in the lesions, and finally suppress the progression of CNV. Briefly, the CNV-targeting characteristic of MRaNPs provided a prerequisite for efficient CNV intervention, which was attributed to its macrophage-disguised property and the consequent reduced RES uptake.

3.7. In vivo CNV inhibition and inflammation suppression efficacy

To date, most ophthalmic drugs are administered topically since it is noninvasive and convenient. Several studies have reported the application of Rapa eye drops in the treatment of ocular surface diseases[56,57]. Cholkar et al.[58] developed micellar drops to deliver Rapa to the back of eye, but the *in vivo* therapeutic effects have not been explored yet. We therefore prepared Rapa eye drops to investigate the therapeutic efficacy of this formulation in the LCNV model. As a result, it showed little effectiveness in decreasing CNV formation (Supporting Information Fig. S15). Perhaps suffering from low bioavailability for the natural barriers (*i.e.*, the cornea, the vitreous and the inner limiting membrane) and various elimination mechanisms (*i.e.*, tear turnover, nasolacrimal drainage and enzymatic degradation), the usage of topical

Rapa formulation is yet limited in the treatment of angiogenesis-related posterior segment eye diseases[59]. Herein, intravenous delivery of MRaNP may be a potential alternative to address these issues.

To optimize the dosage regimen and maximize the efficacy of MRaNP, we observed the natural time-course of CNV formation and macrophage infiltration at various points in time after laser treatment. The CNV lesions and macrophages in the flat-mounted RCCs were counter-stained with IB4 (green) and F4/80 (a macrophage marker, red), respectively (Supporting Information Fig. S16A). Quantification analysis of CNV areas demonstrated that the formation of CNV peaked on Day 7 and then started to regression (Fig. S16B). Simultaneously, macrophages rapidly infiltrated the CNV lesions on Day 1, peaked on Day 5 and then started to decrease, but were still abundantly present on Day 7. On Day 14, macrophages were slightly infiltrated (Fig. S16C). These results suggested that macrophages played a vigorous role in CNV development and gradually vanished during CNV regression in LCNV model; therefore, the optimum time point to intervene CNV efficiently by MRaNP was within the first 7 days after laser treatment, beyond which the CNV-targeting ability would be decreased.

Having confirmed the favorably increased accumulation of MRaNPs within CNV lesions and optimized the prescription, we then studied the therapeutic efficacy of MRaNPs using the LCNV mouse model. The schematic of the experiment protocol was shown in Fig. 5B: after the laser treatment, the mice were daily intravenously injected with saline, free Rapa, RaNPs or MRaNPs for 7 consecutive days. On Day 8, the mice were sacrificed for further analysis. The size of CNV lesions were assessed by fluorescent imaging of flat-mounted RCCs stained with IB4 (28−32 laser points in each group). Compared with mice in the saline group, mice in the free Rapa, RaNP or MRaNP group showed decreased lesion areas. More importantly, MRaNPs exhibited the greatest anti-angiogenesis activity (Fig. 5C). Quantitative analysis revealed that mice treated with MRaNPs showed significantly reduced CNV area by 65.7%, 54.6% and 50.3% compared with those treated with saline, free Rapa and RaNPs, respectively (Fig. 5D). Similar results were obtained with regard to the anti-inflammation efficacy of different formulations. As shown in Fig. 5E and Supporting Information Fig. S17, the MRaNP-treated mice demonstrated the strongest alleviation of inflammation in the RCCs, regarding to the expression level of proinflammatory cytokines IL-1β, TNF-α and IL-6 (Fig. 5E and Supporting Information Fig S18). Taken together, intravenous injection of MRaNPs could more effectively target CNV lesions and provide higher efficiency in inhibiting CNV and inflammation while avoiding the intravitreal injection-related complications.

3.8. In vivo mechanisms of retinal microenvironment remodeling

Next, the potential molecular mechanisms involved in CNV inhibition and *via* the mTOR signaling pathway were studied. WB analysis showed that there was a significantly increased expression of VEGFA, a dominant pro-angiogenic factor, in the RCCs of the LCNV mice. Besides, Rapa treatment did suppress VEGFA production, particularly in mice treated with MRaNPs (Fig. 6A and Fig. S18). Because VEGFA was one of the downstream targets and effectors of mTOR as demonstrated by the *in vitro* studies[60], we further investigated whether the mTOR signaling pathway was increased in LCNV mice and could be mediated by MRaNPs. Compared with the normal group
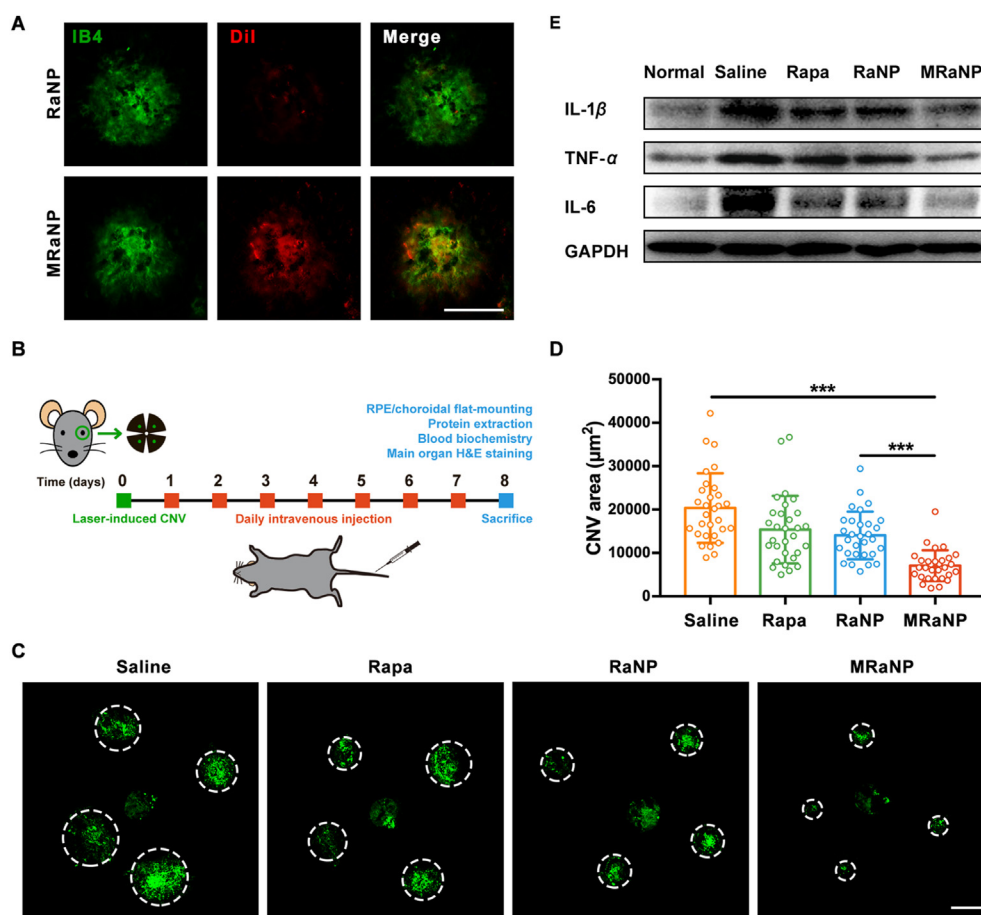
Figure 5 The *In vivo* CNV-targeting ability, anti-angiogenesis effect, and anti-inflammation effect of MRaNPs. (A) Representative fluorescence images of flat-mounted RCCs showing DiI-labeled nanoparticles (red) in CNV areas stained by IB4 (green). Scale bar = 100 μm. (B) Experimental workflow of drug efficacy evaluation. (C) Representative fluorescence images of in CNV areas stained by IB4 (green) after different treatments. Dashed lines delineate the lesion. Scale bar = 100 μm. (D) Quantitation analysis of CNV areas after different treatments (28−32 laser points each group, ***$P < 0.001$). (E) WB analysis for proinflammatory cytokines in RCCs after different treatments.

without laser treatment, elevated phosphorylation of m-TOR (Ser2448), P70S6K (Thr389) and S6 (Ser240/244) was observed in the saline group, suggesting that the mTOR pathway was indeed upregulated during CNV progression. Furthermore, such activation effect was counteracted by Rapa intervention, particularly in the MRaNP group (Fig. 6A and Fig. S18). Similar results were also obtained in co-immunostaining of IB4 and p-mTOR in flat-mounted RCCs: mice in the MRaNP group exhibited the minimal CNV area and the lowest phosphorylation level of m-TOR (Fig. 6B and C). These results were consistent with the current knowledge about the role of mTOR signaling pathway in angiogenesis[47,60−62]. Accordingly, it was suggested that MRaNPs efficiently attenuated the progression of CNV by mediating VEGFA production through the mTOR signaling pathway.

Since RPE is the principal source of VEGFA and nanoparticles with negative surface were easier to travel through the choroid and retina, the drastically reduced production of VEGFA in MRaNP group also indicated that MRaNPs could deliver Rapa beyond the choroidal vasculature layer to the adjacent RPE layer to modulate RPE function (Fig. 1A). As *in vitro* studies suggested that MRaNPs could alleviate inflammation by inducing autophagy, this

mechanism was next verified *in vivo* in the LCNV mouse model, which was also relied on inflammation[34]. To this aim, WB analysis was employed to investigate the autophagic flux in the RCCs by detecting three autophagy-related proteins Beclin-1, P62 and LC3 in RCCs. Compared with the normal mice, the increased expression of Beclin-1, a key regulator of autophagosome formation, in LCNV mice reflected the increased number of autophagosome for degradation of the harmful organelles in response to inflammation (Fig. 6D and Supporting Information Fig. S19). However, mice in the saline group showed apparent accumulation of undegraded P62, which indicated that the complete autophagic flux was impaired by inflammatory injury (Fig. 1B). Even intervention by free Rapa or RaNPs failed to improve it. Luckily, MRaNP treatment was sufficient to promote P62 degradation, indicating the restoration of the autophagic flux (Fig. 6D). In line with these results, the highest ratio between the two forms of LC3 (measured as LC3-II/LC3-I) in the MRaNP group demonstrated that there was a substantially increased autophagy activity in this group compared with other groups (Fig. 6D and E). These results were in consistence with what was observed *in vitro*, confirming the implement of Rapa delivery to the RPE by MRaNPs. Given the
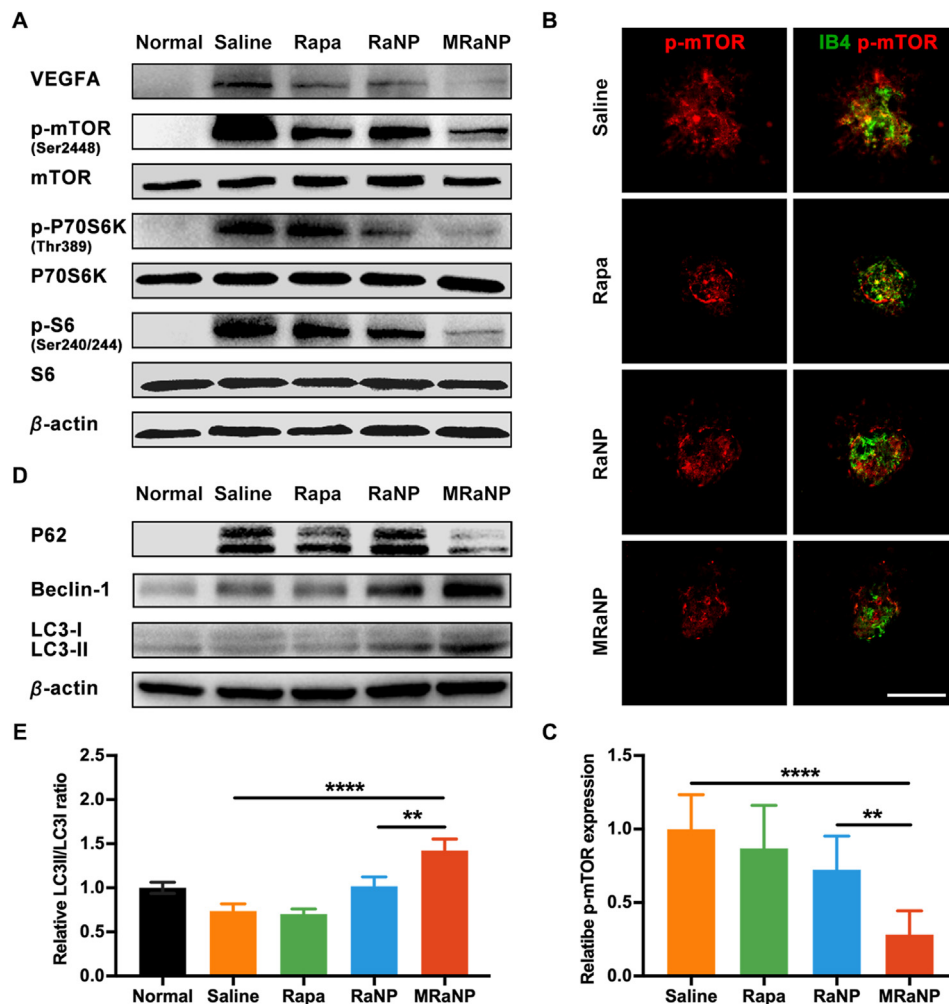
Figure 6 *In vivo* angiogenesis inhibition and autophagy activation effects of MRaNPs *via* the mTOR signaling pathway. (A) WB analysis for VEGFA and the mTOR signaling pathway in RCCs. (B) Representative fluorescence images of immunostaining of p-mTOR (red) in CNV areas stained by IB4 (green). Scale bar = 100 μm. (C) Quantitation analysis of the p-mTOR fluorescence intensity in CNV areas ($n = 3$, $**P < 0.01$ and $****P < 0.0001$). (D) WB analysis for autophagy-associated proteins in RCCs. (E) Semi-quantitation analysis of the LC3-II/-I ratio ($n = 3$, $**P < 0.01$ and $****P < 0.0001$).

inefficient autophagy in various AMD-like phenotypic mouse models[53,63,64], it was reasonable to presume that MRaNPs could protect RPE from excessive inflammation by upregulating autophagy upon inhibiting the mTOR signaling pathway.

3.9.   Biosafety assessment

To assess the biosafety, the blood of LCNV mice was collected to determine the liver function biomarkers (AST and ALT), kidney function biomarkers (CREA and URAS) and nutritional markers (ALB and ALP) on Day 8. The above-mentioned biochemical markers did not vary between the control group (saline) and groups daily treated with free Rapa, RaNPs of MRaNPs (Fig. 7A–F). Histological study by hematoxylin and eosin (H&E) staining revealed no significant pathological changes in the retina (Fig. 7G). Additionally, the main organs including the heart, liver, spleen, lung and kidney revealed normal histology and did not show any distinguishable differences between groups (Fig. 7H, Supporting Information Figs. S19 and S20). The favorable biocompatibility of MRaNPs was predictable, which was attributed to the relative

low dose of Rapa and the rational design employing biocompatible materials, including PLGA and natural cell membrane.

4.   Discussion

Although the molecular mechanism that leads to AMD is poorly understood, we have realized that dysfunction and loss of RPE is central to the disease progression and the manifestation of CNV is a critical time bomb requesting urgent intervention[4,65]. The mTOR signal pathway has proved to be activated both in RPE degeneration and CNV development, suggesting the therapeutic potential of mTOR inhibition for AMD. Despite of the multiple pharmaceutical effects of the mTOR inhibitor Rapa, including but not limited to anti-inflammation, anti-angiogenesis and inducing autophagy, it is yet to be clinically applied owing to the adverse effects *via* topical administration and the off-target effects *via* systemic administration[12,19,20]. In the current study, we described a biomimetic macrophage-membrane-based Rapa delivery vehicle to home towards the CNV lesion sites *via* the intravenous route, which not only prevents the risks of repeated intravitreal injections, but also offers superiorities in
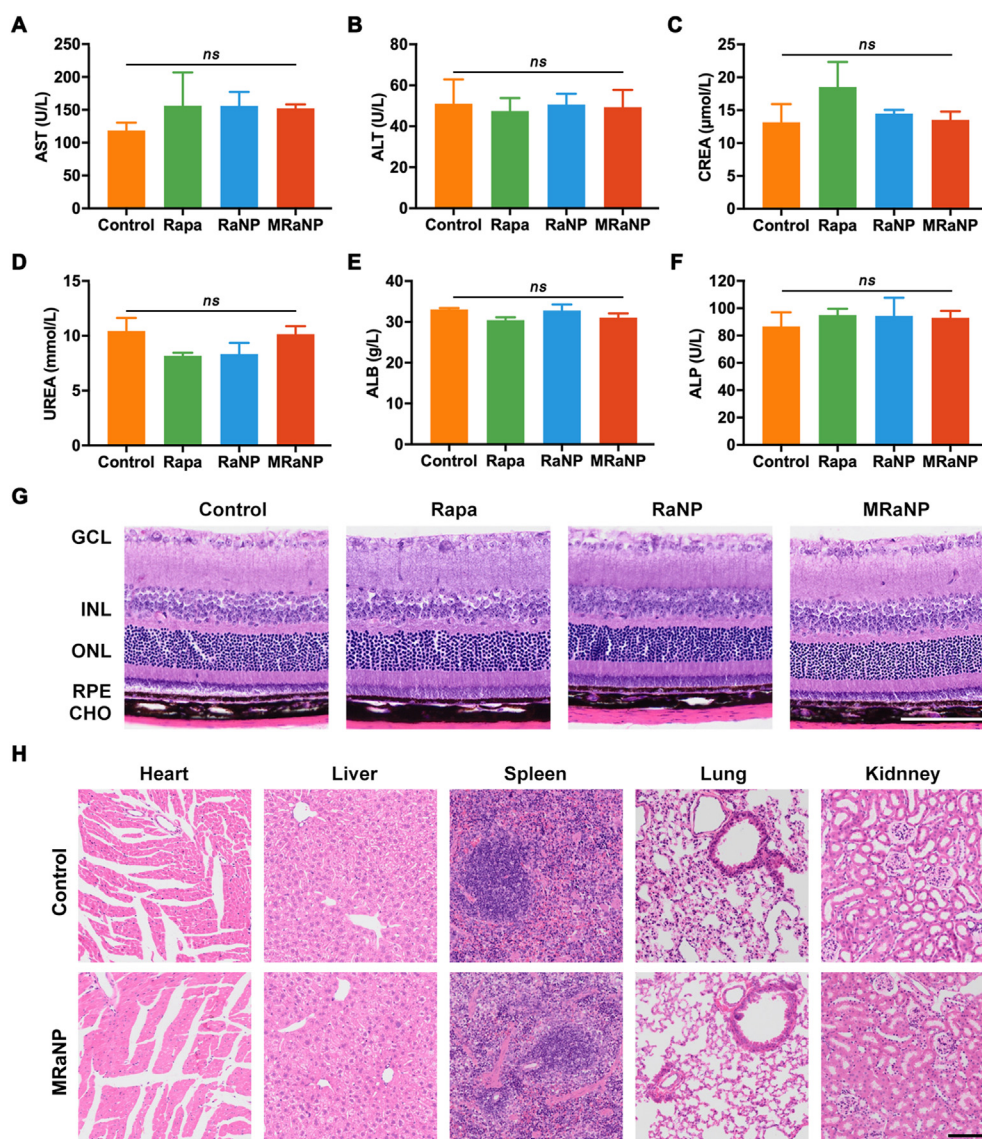
Figure 7 Biocompatibility and safety of MRaNPs. The results of AST (A), ALT (B), CREA (C), UREA (D), ALB (E) and ALP (F) examinations after different treatments for 7 days ($n = 3$, *ns*, no statistical significance). H&E staining of retina (G) and major organs (H) after different treatments indicated no tissue damage on Day 8. CHO, choroid; ONL, outer nuclear layer; INL, inner nuclear layer; GCL, ganglion cells layer. Scale bar = 100 μm.

targeted drug delivery, favorable BRB penetration and prolonged retention time. In agreement with this point, another recent study demonstrated that intravenously administered hybrid membrane-coated nanoparticles are advantageous to reducing the area of CNV by absorbing pro-angiogenic factors[66]. Beyond attenuating angiogenesis, in this study, the loaded Rapa also indicated a potential effect of rescuing RPE by enhancing autophagy, which might address the underlying cause of AMD. Therefore, the plausible mechanisms of MRaNP remodeling retinal homeostasis were summarized as following: under the inflammatory milieu of LCNV, MRaNPs could disguise as macrophages, pass through the impaired BRB and accumulate in the lesion regions, thus improving the bioavailability of Rapa for angiogenesis inhibition, inflammation suppression and autophagy enhancement. A virtuous circle could thereby be developed within the inflammatory microenvironment to eventually diminish inflammation and restore retinal homeostasis (Fig. 1B).

5. Conclusions

In summary, CNV-targeting delivery of Rapa *via* the noninvasive intravenous route may offer an alternative therapeutic strategy, or at least solve the deficiencies of current anti-VEGF therapy to slow or prevent AMD progression. This work also opens the door of posterior ocular drug delivery by employing biomimetic cell membrane-based nanocarriers.

Author contributions

Conflicts of interest

The authors have no conflicts of interest to declare.

Appendix A. Supporting information

Supporting data to this article can be found online at https://doi.org/10.1016/j.apsb.2021.10.022.

References

1. Chakravarthy U, Peto T. Current perspective on age-related macular degeneration. *JAMA* 2020;**324**:794−5.
2. Somasundaran S, Constable IJ, Mellough CB, Carvalho LS. Retinal pigment epithelium and age-related macular degeneration: a review of major disease mechanisms. *Clin Exp Ophthalmol* 2020;**48**:1043−56.
3. Mitchell P, Liew G, Gopinath B, Wong TY. Age-related macular degeneration. *Lancet* 2018;**392**:1147−59.
4. Wong WL, Su XY, Li X, Cheung CM, Klein R, Cheng CY, et al. Global prevalence of age-related macular degeneration and disease burden projection for 2020 and 2040: a systematic review and meta-analysis. *Lancet Glob Health* 2014;**2**:e106−16.
5. Kauppinen A, Paterno JJ, Blasiak J, Salminen A, Kaarniranta K. Inflammation and its role in age-related macular degeneration. *Cell Mol Life Sci* 2016;**73**:1765−86.
6. Murakami Y, Ishikawa K, Nakao S, Sonoda KH. Innate immune response in retinal homeostasis and inflammatory disorders. *Prog Retin Eye Res* 2020;**74**:100778.
7. Antikainen H, Driscoll M, Haspel G, Dobrowolski R. TOR-mediated regulation of metabolism in aging. *Aging Cell* 2017;**16**:1219−33.
8. Zhao C, Yasumura D, Li XY, Matthes M, Lloyd M, Nielsen G, et al. mTOR-mediated dedifferentiation of the retinal pigment epithelium initiates photoreceptor degeneration in mice. *J Clin Invest* 2011;**121**:369−83.
9. Saint-Geniez M, Kurihara T, Sekiyama E, Maldonado AE, D'Amore PA. An essential role for RPE-derived soluble VEGF in the maintenance of the choriocapillaris. *Proc Natl Acad Sci U S A* 2009;**106**:18751−6.
10. Park TK, Lee SH, Choi JS, Nah SK, Kim HJ, Park HY, et al. Adeno-associated viral vector-mediated mtor inhibition by short hairpin RNA suppresses laser-induced choroidal neovascularization. *Mol Ther Nucleic Acids* 2017;**8**:26−35.
11. Kaarniranta K, Sinha D, Blasiak J, Kauppinen A, Veréb Z, Salminen A, et al. Autophagy and heterophagy dysregulation leads to retinal pigment epithelium dysfunction and development of age-related macular degeneration. *Autophagy* 2013;**9**:973−84.
12. Wang Y, Wang VM, Chan CC. The role of anti-inflammatory agents in age-related macular degeneration (AMD) treatment. *Eye (Lond)* 2011;**25**:127−39.
13. Stewart MW. PDGF: ophthalmology's next great target. *Expet Rev Ophthalmol* 2013;**8**:527−37.
14. Martin DF, Maguire MG, Fine SL, Ying GS, Jaffe GJ, Grunwald JE, et al. Ranibizumab and bevacizumab for treatment of neovascular age-related macular degeneration: two-year results. *Ophthalmology* 2012;**119**:1388−98.
15. Grunwald JE, Pistilli M, Daniel E, Ying GS, Pan W, Jaffe GJ, et al. Incidence and growth of geographic atrophy during 5 years of comparison of age-related macular degeneration treatments trials. *Ophthalmology* 2017;**124**:97−104.
16. Daniel E, Toth CA, Grunwald JE, Jaffe GJ, Martin DF, Fine SL, et al. Risk of scar in the comparison of age-related macular degeneration treatments trials. *Ophthalmology* 2014;**121**:656−66.
17. Lyu QH, Peng L, Hong XQ, Fan TJ, Li JY, Cui YB, et al. Smart nano-micro platforms for ophthalmological applications: the state-of-the-art and future perspectives. *Biomaterials* 2021;**270**:120682.
18. Yerramothu P. New therapies of neovascular AMD-Beyond anti-VEGFs. *Vision (Basel)* 2018;**2**:31.
19. Yang JY, Madrakhimov SB, Ahn DH, Chang HS, Park TK. mTORC1 and mTORC2 are differentially engaged in the development of laser-induced CNV. *Cell Commun Signal* 2019;**17**:64.
20. Zhang J, Bai Y, Huang L, Qi Y, Zhang Q, Li S, et al. Protective effect of autophagy on human retinal pigment epithelial cells against lipofuscin fluorophore A2E: implications for age-related macular degeneration. *Cell Death Dis* 2015;**6**:e1972.
21. Merrill PT, Clark WL, Banker AS, Fardeau C, Franco P, LeHoang P, et al. Efficacy and safety of intravitreal Sirolimus for noninfectious uveitis of the posterior segment: results from the sirolimus study assessing double-masked uveitis treatment (SAKURA) program. *Ophthalmology* 2020;**127**:1405−15.
22. Mudumba S, Bezwada P, Takanaga H, Hosoi K, Tsuboi T, Ueda K, et al. Tolerability and pharmacokinetics of intravitreal Sirolimus. *J Ocul Pharmacol Therapeut* 2012;**28**:507−14.
23. Gensler G, Clemons TE, Domalpally A, Danis RP, Blodi B, Wells 3rd J, et al. Treatment of geographic atrophy with intravitreal Sirolimus: the age-related eye disease study 2 ancillary study. Ophthalmolo. *Retina* 2018;**2**:441−50.
24. Agrahari V, Agrahari V, Mandal A, Pal D, Mitra AK. How are we improving the delivery to back of the eye? Advances and challenges of novel therapeutic approaches. *Expet Opin Drug Deliv* 2017;**14**:1145−62.
25. Coleman HR, Chan CC, Ferris 3rd FL, Chew EY. Age-related macular degeneration. *Lancet* 2008;**372**:1835−45.
26. Du ZJ, Wu XM, Song MX, Li P, Wang L. Oxidative damage induces MCP-1 secretion and macrophage aggregation in age-related macular degeneration (AMD). *Graefes Arch Clin Exp Ophthalmol* 2016;**254**:2469−76.
27. Caicedo A, Espinosa-Heidmann DG, Piña Y, Hernandez EP, Cousins SW. Blood-derived macrophages infiltrate the retina and activate Muller glial cells under experimental choroidal neovascularization. *Exp Eye Res* 2005;**81**:38−47.
28. Paschalis EI, Lei FY, Zhou CX, Kapoulea V, Dana R, Chodosh J, et al. Permanent neuroglial remodeling of the retina following infiltration of CSF1R inhibition-resistant peripheral monocytes. *Proc Natl Acad Sci U S A* 2018;**115**:E11359−68.
29. Weber C, Fraemohs L, Dejana E. The role of junctional adhesion molecules in vascular inflammation. *Nat Rev Immunol* 2007;**7**:467−77.
30. Zhang Y, Cai KM, Li C, Guo Q, Chen QJ, He X, et al. Macrophage-membrane-coated nanoparticles for tumor-targeted chemotherapy. *Nano Lett* 2018;**18**:1908−15.
31. Wang Y, Zhang K, Qin X, Li TH, Qiu JH, Yin TY, et al. Biomimetic nanotherapies: red blood cell based core−shell structured nanocomplexes for atherosclerosis management. *Adv Mater* 2019;**6**:1900172.
32. Thamphiwatana S, Angsantikul P, Escajadillo T, Zhang QZ, Olson J, Luk BT, et al. Macrophage-like nanoparticles concurrently absorbing endotoxins and proinflammatory cytokines for sepsis management. *Proc Natl Acad Sci U S A* 2017;**114**:11488−93.
33. Chen YW, Shen WL, Tang CQ, Huang JY, Fan CM, Yin Z, et al. Targeted pathological collagen delivery of sustained-release rapamycin to prevent heterotopic ossification. *Sci Adv* 2020;**6**:eaay9526.
34. Lambert V, Lecomte J, Hansen S, Blacher S, Gonzalez ML, Struman I, et al. Laser-induced choroidal neovascularization model

to study age-related macular degeneration in mice. *Nat Protoc* 2013; **8**:2197−211.

35. Gong Y, Li J, Sun Y, Fu ZJ, Liu CH, Evans L, et al. Optimization of an image-guided laser-induced choroidal neovascularization model in mice. *PLoS One* 2015;**10**:e0132643.

36. Yeh DC, Bula DV, Miller JW, Gragoudas ES, Arroyo JG. Expression of leukocyte adhesion molecules in human subfoveal choroidal neovascular membranes treated with and without photodynamic therapy. *Invest Ophthalmol Vis Sci* 2004;**45**:2368−73.

37. Mullins RF, Skeie JM, Malone EA, Kuehn MH. Macular and peripheral distribution of ICAM-1 in the human choriocapillaris and retina. *Mol Vis* 2006;**12**:224−35.

38. Klein R, Myers CE, Cruickshanks KJ, Gangnon RE, Danforth LG, Sivakumaran TA, et al. Markers of inflammation, oxidative stress, and endothelial dysfunction and the 20-year cumulative incidence of early age-related macular degeneration: the Beaver Dam Eye Study. *JAMA Ophthalmol* 2014;**132**:446−55.

39. Meerschaert J, Furie MB. Monocytes use either CD11/CD18 or VLA-4 to migrate across human endothelium *in vitro*. *J Immunol* 1994;**152**: 1915−26.

40. Meerschaert J, Furie MB. The adhesion molecules used by monocytes for migration across endothelium include CD11a/CD18, CD11b/CD18, and VLA-4 on monocytes and ICAM-1, VCAM-1, and other ligands on endothelium. *J Immunol* 1995;**154**:4099−112.

41. Kevil CG, Patel RP, Bullard DC. Essential role of ICAM-1 in mediating monocyte adhesion to aortic endothelial cells. *Am J Physiol Cell Physiol* 2001;**281**:C1442−7.

42. Nagata M, Sedgwick JB, Vrtis R, Busse WW. Endothelial cells upregulate eosinophil superoxide generation *via* VCAM-1 expression. *Clin Exp Allergy* 1999;**29**:550−61.

43. Behrendt D, Ganz P. Endothelial function. From vascular biology to clinical applications. *Am J Cardiol* 2002;**90**:40l−8l.

44. Lentsch AB, Ward PA. Regulation of inflammatory vascular damage. *J Pathol* 2000;**190**:343−8.

45. Datta S, Cano M, Ebrahimi K, Wang L, Handa JT. The impact of oxidative stress and inflammation on RPE degeneration in non-neovascular AMD. *Prog Retin Eye Res* 2017;**60**:201−18.

46. Leung KW, Barnstable CJ, Tombran-Tink J. Bacterial endotoxin activates retinal pigment epithelial cells and induces their degeneration through IL-6 and IL-8 autocrine signaling. *Mol Immunol* 2009;**46**:1374−86.

47. Wei J, Jiang H, Gao HR, Wang GJ. Blocking mammalian target of rapamycin (mTOR) attenuates HIF-1α pathways engaged-vascular endothelial growth factor (VEGF) in diabetic retinopathy. *Cell Physiol Biochem* 2016;**40**:1570−7.

48. Mayerhofer M, Valent P, Sperr WR, Griffin JD, Sillaber C. BCR/ABL induces expression of vascular endothelial growth factor and its transcriptional activator, hypoxia inducible factor-1alpha, through a pathway involving phosphoinositide 3-kinase and the mammalian target of rapamycin. *Blood* 2002;**100**:3767−75.

49. Golestaneh N, Chu Y, Xiao YY, Stoleru GL, Theos AC. Dysfunctional autophagy in RPE, a contributing factor in age-related macular degeneration. *Cell Death Dis* 2017;**8**:e2537.

50. Guo Q, Chen QJ, Zhang YJ, Zhou WX, Li XW, Li C, et al. Click-nucleic-acid-containing codelivery system inducing collapse of cellular homeostasis for tumor therapy through bidirectional regulation of autophagy and glycolysis. *ACS Appl Mater Interfaces* 2020;**12**: 57757−67.

51. Baker B, Geng S, Chen KQ, Diao N, Yuan RX, Xu XG, et al. Alteration of lysosome fusion and low-grade inflammation mediated by super-low-dose endotoxin. *J Biol Chem* 2015;**290**:6670−8.

52. Kumar MV, Nagineni CN, Chin MS, Hooks JJ, Detrick B. Innate immunity in the retina: toll-like receptor (TLR) signaling in human retinal pigment epithelial cells. *J Neuroimmunol* 2004;**153**:7−15.

53. Yao JY, Jia L, Khan N, Lin CM, Mitter SK, Boulton ME, et al. Deletion of autophagy inducer RB1CC1 results in degeneration of the retinal pigment epithelium. *Autophagy* 2015;**11**:939−53.

54. Macias-Ceja DC, Cosín-Roger J, Ortiz-Masiá D, Salvador P, Hernández C, Esplugues JV, et al. Stimulation of autophagy prevents intestinal mucosal inflammation and ameliorates murine colitis. *Br J Pharmacol* 2017;**174**:2501−11.

55. Zhou MX, Xu WM, Wang JZ, Yan JK, Shi YY, Zhang C, et al. Boosting mTOR-dependent autophagy *via* upstream TLR4-MyD88-MAPK signalling and downstream NF-κB pathway quenches intestinal inflammation and oxidative stress injury. *EBioMedicine* 2018;**35**:345−60.

56. Wei C, Wang YX, Ma L, Wang X, Chi H, Zhang S, et al. Rapamycin nano-micelle ophthalmic solution reduces corneal allograft rejection by potentiating myeloid-derived suppressor cells' function. *Front Immunol* 2018;**9**:2283.

57. Shah M, Edman MC, Reddy Janga S, Yarber F, Meng Z, Klinngam W, et al. Rapamycin eye drops suppress lacrimal gland inflammation in a murine model of Sjögren's syndrome. *Invest Ophthalmol Vis Sci* 2017; **58**:372−85.

58. Cholkar K, Gunda S, Earla R, Pal D, Mitra AK. Nanomicellar topical aqueous drop formulation of rapamycin for back-of-the-eye delivery. *AAPS PharmSciTech* 2015;**16**:610−22.

59. Peynshaert K, Devoldere J, De Smedt SC, Remaut K. *In vitro* and *ex vivo* models to study drug delivery barriers in the posterior segment of the eye. *Adv Drug Deliv Rev* 2018;**126**:44−57.

60. Klos KS, Wyszomierski SL, Sun MH, Tan M, Zhou XY, Li P, et al. ErbB2 increases vascular endothelial growth factor protein synthesis *via* activation of mammalian target of rapamycin/p70S6K leading to increased angiogenesis and spontaneous metastasis of human breast cancer cells. *Cancer Res* 2006;**66**:2028−37.

61. Yao A, Wijngaarden PV. Metabolic pathways in context: mTOR signalling in the retina and optic nerve - a review. *Clin Exp Ophthalmol* 2020;**48**:1072−84.

62. Liu NN, Zhao N, Cai N. Suppression of the proliferation of hypoxia-induced retinal pigment epithelial cell by rapamycin through the/mTOR/HIF-1α/VEGF/signaling. *IUBMB Life* 2015;**67**:446−52.

63. Kaur G, Tan LX, Rathnasamy G, La Cunza N, Germer CJ, Toops KA, et al. Aberrant early endosome biogenesis mediates complement activation in the retinal pigment epithelium in models of macular degeneration. *Proc Natl Acad Sci U S A* 2018;**115**:9014−9.

64. Chen Y, Sawada O, Kohno H, Le YZ, Subauste C, Maeda T, et al. Autophagy protects the retina from light-induced degeneration. *J Biol Chem* 2013;**288**:7506−18.

65. Bhutto I, Lutty G. Understanding age-related macular degeneration (AMD): relationships between the photoreceptor/retinal pigment epithelium/Bruch's membrane/choriocapillaris complex. *Mol Aspect Med* 2012;**33**:295−317.

66. Li MJ, Xu ZJ, Zhang L, Cui MY, Zhu MH, Guo Y, et al. Targeted noninvasive treatment of choroidal neovascularization by hybrid cell-membrane-cloaked biomimetic nanoparticles. *ACS Nano* 2021;**15**: 9808−19.